

Unconventional superconductivity from lattice quantum disorder

Yu-Cheng Zhu,¹ Jia-Xi Zeng,¹ and Xin-Zheng Li^{1, 2, *}

¹*State Key Laboratory for Artificial Microstructure and Mesoscopic Physics,
Frontier Science Center for Nano-optoelectronics and School of Physics,
Peking University, Beijing 100871, People's Republic of China*

²*Interdisciplinary Institute of Light-Element Quantum Materials,
Research Center for Light-Element Advanced Materials,
and Collaborative Innovation Center of Quantum Materials,
Peking University, Beijing 100871, People's Republic of China*

(Dated: February 4, 2026)

Unconventional superconductivity presents a defining and enduring challenge in condensed matter physics. Prevailing theoretical frameworks have predominantly emphasized electronic degrees of freedom, largely neglecting the rich physics inherent in the lattice. Although conventional phonon theory offers an elegant description of structural phase diagrams and lattice dynamics, its omission of nuclear quantum many-body effects results in misleading phase diagram interpretations and, consequently, an unsound foundation for superconducting theory. Here, by incorporating nuclear quantum many-body effects within first-principles calculations, we discover a lattice quantum disordered phase in superconductors H_3S and $\text{La}_3\text{Ni}_2\text{O}_7$. This phase occupies a triangular region in the pressure–temperature phase diagram, whose left boundary aligns precisely with T_c of the left flank of the superconducting dome. The T_c^{\max} of this quantum disordered phase coincides with the maximum of superconducting T_c , indicating this phase as both the origin of superconductivity on the dome's left flank and a key ingredient of its pairing mechanism. Our findings advance the understanding of high-temperature superconductivity and establish the lattice quantum disordered phase as a unifying framework, both for predicting new superconductors and for elucidating phenomena in a broader context of condensed matter physics.

The left flank of the superconducting dome—spanning the underdoped or low-pressure regime up to the peak T_c —is pivotal for deciphering the mechanism of high-temperature superconductivity[1–3]. This region is characterized by an intimate entanglement of magnetic, charge, and structural orders[4, 5]. While such complexity has inspired influential theoretical paradigms, including those based on magnetic fluctuations and strong electron correlations, it has also led to a lack of consensus, obscuring a unified physical picture[6, 7]. The growing family of unconventional superconductors[8] and advances in first-principles methods[9] now highlight structural phase transitions as a clarifying lens, given their universal link to competing orders and their essential role in ab initio modeling. Nevertheless, prevailing theoretical approaches remain predominantly electron-centric, largely overlooking the rich and decisive physics of the lattice.

Recent studies of high-pressure superconductors have opened new avenues for understanding high-temperature superconductivity, bringing structural phase transitions into sharp focus[10–18]. In such systems, nuclear quantum effects are known to reshape superconducting phase diagrams by altering structural boundaries[19, 20]. A prominent example is H_3S , where accounting for these effects dramatically lowers the pressure for hydrogen-bond symmetrization relative to classical predictions, shifting the entire superconducting dome into the $\text{Im}\bar{3}\text{m}$ phase and challenging the prior two-phase interpretation[19, 21]. While such studies incorporated essential quantum

corrections, they did not fully address the many-body nature of the interacting nuclei. In our recent work, by rigorously including nuclear quantum many-body effects within a first-principles framework, we have achieved a more accurate determination of the structural phase boundaries and, significantly, revealed a lattice quantum disordered (LQD) phase[22]. In this regime, quantum fluctuations stabilize a higher-symmetry disordered state, giving rise to lattice dynamics beyond the conventional phonon picture. This finding not only redefines the structural phase diagram but also directly motivates the present investigation into the link between such quantum lattice disorder and the unresolved physics on the left flank of the T_c dome. The recent discovery of nickel-based superconductors, accompanied by enhanced structural characterization under pressure, provides a timely platform for validating this picture[10–14, 23].

Here, we find that the superconducting transition on the left flank of the dome stems from the structural transition of a low-symmetry phase into a LQD phase. We employ path-integral molecular dynamics (PIMD)[25, 26] to treat the nuclear quantum many-body effects from first principles. The structural phase boundary is determined by the free-energy surface, which is constructed by the centroid potential of mean force from PIMD. The boundary obtained via this approach coincides precisely with the left flank of the superconducting dome. Its intersection with the classical boundary from conventional molecular dynamics delineates the region of the LQD phase. The extent of this LQD phase increases linearly

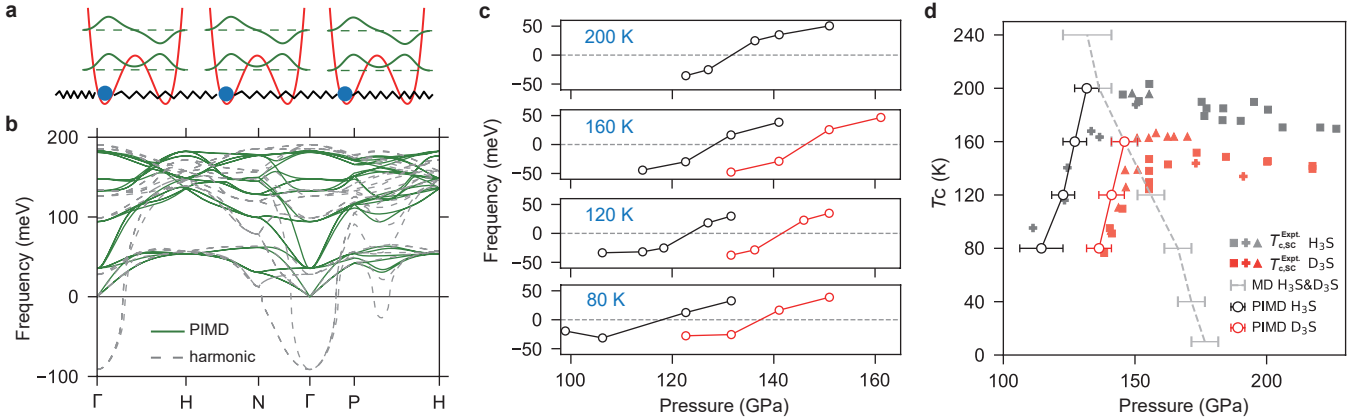


FIG. 1: Lattice quantum disordered phase in H_3S and D_3S from first-principles calculation. **a**, A schematic diagram of a 1-D double-well chain, which describes the LQD phase. The nucleus on each lattice site (the ball) lies on a double-well potential (red curve) connected to the neighboring sites by spring interactions (zigzag lines). The many-body nuclear quantum states are determined by the competition between the on-site tunneling effects and the inter-site interactions. In Ref. 22, we have a detailed description of the LQD phase described by this model and the PIMD method. **b**, The dispersion relation of lattice dynamics of $\text{Im}\bar{3}\text{m}$ H_3S ($T = 200$ K, $P = 141$ GPa) by PIMD (solid lines) in comparison with the harmonic phonon spectra (dashed lines). The structural instability indicated by the soft phonon mode is suppressed. **c**, PIMD frequency at Γ point for the soft mode defined in (b), as a function of temperature and pressure. The open black and red circles correspond to H_3S and D_3S , respectively. The structural phase transition is defined by the point at which this frequency changes sign. **d**, The triangular region of the LQD phase on the $P - T$ phase diagram is bounded by the quantum (PIMD) and classical (MD) phase boundaries. The solid symbols represent the experimental superconducting $T_{c,\text{SC}}$ from Refs. [16, 20, 24]. Notably, the left boundary of the LQD phase (the PIMD line) aligns with the left flank of the superconducting dome, and $T_{c,\text{LQD}}^{\text{max}}$ coincides with $T_{c,\text{SC}}^{\text{max}}$ for both H_3S and D_3S .

with decreasing temperature, with its origin, which we label as $T_{c,\text{LQD}}^{\text{max}}$, locating at ~ 220 K for H_3S , ~ 160 K for D_3S and ~ 77 K for $\text{La}_3\text{Ni}_2\text{O}_7$. These values align exactly with their respective highest observed superconducting transition temperatures $T_{c,\text{SC}}^{\text{max}}$. This indicates not only that superconductivity occurs entirely within the high-symmetry phase but also establishes a direct mechanistic link between the LQD phase and unconventional superconductivity. We expect this picture to be broadly applicable to other unconventional superconductors.

LQD phase by PIMD

Thermal and quantum fluctuations are key factors that can suppress a structural phase transition. A soft phonon mode in the potential energy surface (PES) does not necessarily imply a structural instability in the free energy surface (FES) once these fluctuations are included. Thus, the true phase transition point must be identified by examining the curvature of the FES that fully accounts for both thermal and quantum effects. This offers a fundamental and broadly applicable criterion for structural instability. While thermal fluctuations are well described by conventional molecular dynamics (MD), the key challenge lies in correctly including nuclear quantum

effects[27] when calculating the FES.

At low temperatures, when the potential barrier of a soft mode is modest, nuclear tunneling induces strong quantum fluctuations (sketched by the green wavefunctions of double-well potential in Fig. 1a) that favor a quantum disordered state[22]. In competition, there is a global tendency for all lattice sites to slide toward the same side of the potential well (as the blue balls) to lower the energy, thereby establishing long-range structural order. The resulting transition from a low-symmetry to a high-symmetry phase is therefore a quantum order-disorder transition[28], governed by the balance between quantum fluctuations and long-range ordering (effect of inter-site interaction as the zigzag springs)[22]. This physics necessitates a treatment that captures the many-body nature of the quantum nuclei.

To this end, we employ path-integral molecular dynamics (PIMD), a powerful framework for including such nuclear quantum many-body effects and the thermal effects[25–27, 29]. Within PIMD, the centroid potential of mean force provides a rigorous route to construct the relevant FES[30, 31]. Leveraging lattice symmetry, the emergence of a soft mode—and hence the phase boundary—can be determined efficiently from the centroid effective forces of only a few finite-displaced struc-

tures. The region between this quantum phase boundary and the classical boundary from MD defines the LQD phase. In the following, we apply this approach to map the LQD phase in two representative systems: H_3S and $La_3Ni_2O_7$. To make the PIMD sampling feasible, we employ machine learning inter-atomic potentials at the density-functional theory (DFT) level[32, 33] as the PES, with the underlying DFT calculations performed using the PBE functional[34]. The computational details are provided in the Methods section.

H_3S

The lattice dispersion obtained via the centroid effective forces (Fig. 1b) show that imaginary harmonic frequencies—indicating a saddle point in the PES—are suppressed in the PIMD spectrum when quantum fluctuations are strong. Tracking the soft-mode frequency at the Γ point across pressure and temperature (Fig. 1c) allows us to locate the phase boundary where this frequency changes sign. The resulting boundary shifts to higher pressure with increasing temperature (Fig. 1d), in contrast to the classical trend and to other quantum correction methods[35] (see Extended Data Fig. 1). This arises from two competing influences: thermal and quantum effects both suppress structural order, but thermal agitation also disrupts quantum effects, rapidly diminishing the LQD phase. Consequently, the structural phase boundary in the $T - P$ plane forms a dome: it first rises with temperature before eventually crossing over to the classical regime.

The classical boundary, identified from the pair distribution function via MD (Extended Data Fig. 2), together with the PIMD quantum boundary, delineates a triangular LQD region. Their intersection defines the $T_{c,LQD}^{\max}$ of the LQD phase—the temperature at which quantum effects are completely overwhelmed by thermal fluctuations. Due to the greater mass of deuterium compared to hydrogen, its quantum effects are weaker. As a result, the quantum phase boundary of D_3S shifts to higher pressures, and its $T_{c,LQD}^{\max}$ is about 160 K, which is lower than the 220 K for H_3S as in Fig. 1d.

In H_3S , the superconducting transition temperature T_c exhibits a characteristic dome in the $P - T$ plane[20]. A distinct, continuous kink at the dome's maximum—evident in the experimental data (the gray filled dots in Fig. 1d) and also observed in nickel-based superconductors[10]—provides a natural marker that defines the lower-pressure region (below 150 GPa) as the dome's left flank. The key finding is that the left boundary of the LQD phase aligns with the left flank. Moreover, the isotope effect in superconductivity is accurately captured by the LQD phase. Although the quantitative agreement with experiment is limited by DFT precision (results with other functionals are in the Extended Data Fig. 1), the correspondence between the phase

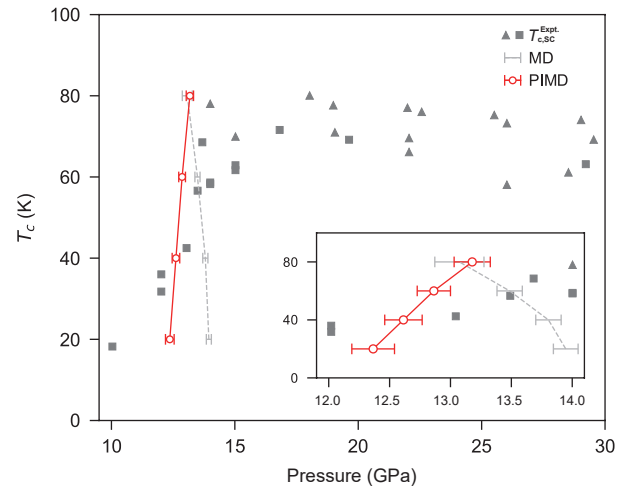


FIG. 2: Lattice quantum disordered phase in $La_3Ni_2O_7$ from first-principles calculation. The solid symbols represent the experimental superconducting $T_{c,SC}$ from Refs. [10, 11]. On the left flank of the superconducting dome (below 14 GPa), $T_{c,SC}$ is marked by a sudden and rapid decrease. The quantum structural phase boundary by PIMD aligns with the left flank, and $T_{c,LQD}^{\max} \approx 77$ K is in consistence with the experimental $T_{c,SC}^{\max} = 80$ K.

boundaries strongly indicates that the superconducting transition on the left flank originates from the LQD phase—and, consequently, that superconductivity occurs entirely within the high-symmetry $Im\bar{3}m$ phase, thereby invalidating earlier two-phase interpretations and the calculations based upon them[36].

A more important point is that the $T_{c,LQD}^{\max}$ coincides precisely with the peak superconducting temperature $T_{c,SC}^{\max}$ for both H_3S and D_3S . This agreement, robust across different exchange-correlation functionals (Extended Data Fig. 1), establishes a direct link between LQD and the superconducting mechanism. Having established this framework for H_3S , we now examine $La_3Ni_2O_7$ to test its generality, before finally presenting a unified picture in the subsequent discussion.

$La_3Ni_2O_7$

Nickel-based superconductors offer a compelling platform to clarify the link between the LQD phase and unconventional superconductivity. In these systems, first-principles calculations have played a central role[10], and the assumed crystal structure—as the starting point of such calculations—directly influences theoretical interpretations of the superconducting mechanism. It is therefore critical to correctly determine the structural phase diagram[12–14]. Current studies suggest a transition from $I4/mmm$ to a lower-symmetry phase around a few

tens of GPa, and—reminiscent of the earlier, erroneous two-phase picture for H_3S —assign the left flank of the superconducting dome to that low-symmetry phase[23]. Here, we resolve the structural transitions in nickel-based superconductors using $\text{La}_3\text{Ni}_2\text{O}_7$ as a representative example, and reveal the relationship between the LQD phase and the superconducting dome. We note that, unlike the earlier studies[10, 37], we do not employ the PBE+U approach because it fails to reproduce the stable structures and yields phase-transition pressures far from experimental values (see Extended Data Fig. 3). For generality and computational feasibility, we use the PBE functional throughout.

As shown in Fig. 2, the left boundary of the LQD phase shifts to higher pressure with increasing temperature, matching the steep left flank of the superconducting dome. Within the precision of DFT, this indicates that—as in H_3S —the left boundary of the LQD phase coincides with the left flank of the dome, and that superconducting transition on this flank originates from the quantum order-disorder transition into the LQD phase. More importantly, the $T_{c,\text{LQD}}^{\text{max}}$ aligns with the $T_{c,\text{SC}}^{\text{max}}$ again. The intersection of the PIMD and MD boundaries gives a maximum T_c of about 77 K for the LQD phase of $\text{La}_3\text{Ni}_2\text{O}_7$ at the PBE level, in consistence with the experimental maximum of superconducting T_c of 80 K.

General phase diagram

Fig. 3 summarizes the proposed picture for the phase diagram. At low temperatures, the structural transition is a quantum order-disorder transition, which shifts the phase boundary to lower pressures compared to the classical limit. Above $T_{c,\text{LQD}}^{\text{max}}$, the system recovers the classical first-order transition behavior. Here, we suggest that experiments aiming to locate this boundary should track the change in lattice parameters and focus on temperatures just above the maximum superconducting T_c rather than at room temperature. The intersection of the quantum and first-order transition lines—which is the $T_{c,\text{LQD}}^{\text{max}}$ —constitutes a tricritical point. Given the observed coincidence between the left boundary of the LQD phase and the left flank of the superconducting dome, we conclude that superconductivity occurs entirely within the high-symmetry phase, thereby refuting earlier two-phase interpretations. Crucially, the LQD phase is distinct from a static high-symmetry phase; its lattice dynamics, which transcend the conventional phonon picture, may host a novel pairing mechanism.

Superconductivity should be viewed not only as a macroscopic quantum state of electronic degrees of freedom, but equally as one of the lattice. The energy scale of lattice dynamics (tens to hundreds of kelvins) is comparable to the T_c of high-temperature superconductors; at the very least, the process by which thermal effects suppress nuclear quantum fluctuations cannot be

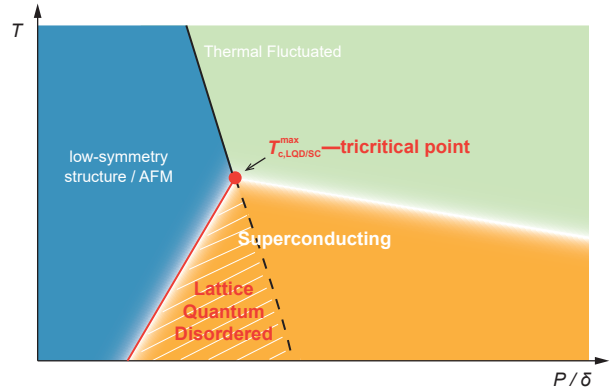


FIG. 3: Schematic phase diagram of lattice quantum disorder and unconventional superconductivity. The quantum order-disorder transition boundary (solid red line), dominant at low temperatures, is shifted to lower pressures compared to the classical transition boundary (dashed black line). Their intersection defines $T_{c,\text{LQD}}^{\text{max}}$ —a tricritical point (red point). The region enclosed by these two boundaries is the LQD phase (shaded orange area). Experimentally observed superconductivity forms a dome (orange area). Crucially, the left flank of the superconducting dome coincides with the left boundary of the LQD phase, and $T_{c,\text{SC}}^{\text{max}}$ aligns precisely with the tricritical point ($T_{c,\text{LQD}}^{\text{max}}$). We contend that this unequivocally points to a superconducting mechanism inherent to the LQD phase, with the tricritical point determining the maximum superconducting transition temperature.

ignored. If one attributes the right flank of the dome to a BCS-like mechanism, where T_c rises slowly with decreasing pressure, the quantum order-disorder transition could be seen as interrupting this rise. However, this cannot explain why the $T_{c,\text{LQD}}^{\text{max}}$ coincides precisely with the $T_{c,\text{SC}}^{\text{max}}$ —that is, why a scenario such as that sketched in Extended Data Fig. 4 does not occur. Based on consistent first-principles results across H_3S and $\text{La}_3\text{Ni}_2\text{O}_7$, we argue that this agreement is not coincidental. We instead propose that the right flank of the dome extends from the tricritical point, indicating a profound connection between LQD and the unconventional superconducting mechanism, with the LQD phase playing a decisive role in determining the maximum superconducting transition temperature.

This picture suggests a practical route for predicting and discovering superconductors with higher T_c : first identify materials that host a large LQD phase, and subsequently consider appropriate carrier introduction. Regarding doping, we expect the LQD framework to remain relevant for doping-dependent high- T_c families such as the cuprates[38]. Notably, the antiferromagnetic phase

(AFM) that competes with superconductivity in these systems often also exhibits a dome shape in the $T - P$ plane[39, 40], suggesting that the AFM phase is coupled to a structural phase transition and the left flank of their superconducting domes may likewise originate from a quantum order-disorder structural transition. Doping may influence the soft mode on the potential energy surface in a manner analogous to pressure, though its combined effect on both the lattice and carrier concentration is more complex and places higher demands on first-principles treatments[41]. Finally, we suggest that the LQD phase could be a widespread phenomenon, with its extent varying across different materials. We anticipate that this perspective will offer fresh insights into other unresolved puzzles in condensed matter, particularly concerning anomalous transport properties such as glass-like thermal conductivity in crystals[42].

Methods

PIMD simulations

We performed fixed-centroid PIMD to obtain the centroid mean force. During the PIMD simulation, the centroid was fixed at a finite-displaced structure and then the mean force was averaged from centroid forces of all the steps in the trajectory. A set of finite-displaced structures (0.03 Å from equilibrium position) were generated according to lattice symmetry by Phonopy software[43]. Then the corresponding set of centroid mean forces were used to construct the force constant, from which we can obtain the dispersion relation. The PIMD simulations were performed using the i-pi software[44] (version 3.1). We used NVT ensemble and Path-integral Langevin equation thermostat. For each centroid mean force, we ran 600,000 steps to ensure a sufficient sampling, with the time step being 0.5 fs. The number of beads N_b was set to ensure $N_b \times T \geq 5,120$ K, specifically, $N_b = 32$ for $T = 200, 160$ K and $N_b = 64$ for $T = 120, 80$ K. For H_3S and D_3S , we simulated in a $3 \times 3 \times 3$ supercell of unit cell containing totally 216 atoms. For $\text{La}_3\text{Ni}_2\text{O}_7$, we simulated in a $2\sqrt{2} \times 2\sqrt{2} \times 1$ supercell containing totally 192 atoms. The convergence on number of beads and size of supercell is shown in Extended Data Fig.5.

Machine-learning potentials at DFT level

The Born-Oppenheimer PES was constructed using a combination of density-functional theory (DFT) and the machine learning inter-atomic potential method. The DFT calculations are performed by the Vienna Ab initio Simulation Package (VASP)[45] at GGA level using the Perdew-Berke-Ernzerhof (PBE) functional[34] and projector augmented wave (PAW) pseudopotentials[46]. The

machine learning techniques are used to save computational cost so that our PIMD simulation is doable[47]. Here we employ the machine-learning force field (MLFF) built in VASP[48, 49]. As a practical test on the training accuracy of the MLFF, the harmonic phonon spectra (by Phonopy software) in comparison with the DFT one are shown in Extended Data Fig. 6. All the atomic simulations in this work including PIMD and MD were performed on the MLFF.

For H_3S , the plane-wave cutoff was set as 550 eV. We used a $8 \times 8 \times 8$ Gamma k -mesh for a $2 \times 2 \times 2$ supercell of unit cell. This unit cell of $\text{Im}\bar{3}\text{m}$ phase contains 8 atoms. We ran MD in the $2 \times 2 \times 2$ supercell containing 64 atoms at 150 GPa, 125 GPa, 100 GPa and 75 GPa, to generate data set for training MLFF. At each pressure, the system was gradually heated from 1 K to 400 K in 25 ps with a time step of 0.5 fs. 3926 configurations were selected from the MD trajectories, constructing the training dataset. To better describe the local environment around each atom, we used a Gaussian broadening of 0.3 Å for atomic distribution function. The standard derivation of the training dataset is 0.18 eV/atom for energy, 0.39 eV/Å for force and 19.0 GPa for stress. The standard error of the MLFF on the dataset is 0.15 meV/atom for energy, 0.02 eV/Å for force and 0.3 GPa for stress.

For $\text{La}_3\text{Ni}_2\text{O}_7$, the plane-wave cutoff was set as 700 eV. We used a $6 \times 6 \times 1$ Gamma k -mesh for a $2 \times 2 \times 1$ supercell of unit cell. This unit cell of $\text{I}4/\text{mmm}$ phase contains 24 atoms. We ran MD in the $2 \times 2 \times 1$ supercell containing 96 atoms at 0 GPa, 10 GPa and 20 GPa, to generate data set for training MLFF. At each pressure, the system was gradually heated from 1 K to 200 K in 100 ps with a time step of 2 fs. 1854 configurations were selected from the MD trajectories, constructing the training dataset. To better describe the local environment around each atom, we used a Gaussian broadening of 0.3 Å for atomic distribution function. The standard derivation of the training dataset is 29.5 meV/atom for energy, 0.30 eV/Å for force and 5.5 GPa for stress. The standard error of the MLFF on the dataset is 0.05 meV/atom for energy, 0.01 eV/Å for force and 0.2 GPa for stress.

Equation of state

The pressure at a specific lattice parameter was determined by conventional (unfixed-centroid) PIMD. The number of beads N_b was set to ensure $N_b \times T \geq 5,120$ K. We used NVT ensemble and Path-integral Langevin Equation thermostat with a local langevin thermostat to the centroid mode[50]. The friction factor was $\tau = 100$ fs. The time step was 0.5 fs. The $P - V$ curves at different T are shown in Extended Data Fig. 7.

Classical boundaries by MD

For H_3S , the classical boundary of the structural phase transition between $\text{Im}\bar{3}\text{m}$ and $\text{R}3\text{m}$ was determined by the pair distribution function (PDF) from MD simula-

tion. For each temperature and volume, we performed a 50 ps MD simulation in the $3 \times 3 \times 3$ supercell. We used the NVT ensemble and the Langevin thermostat, with the friction factor being $\tau = 100$ fs. The S-H PDFs at a range of temperatures and lattice parameters were summarized in the upper panel of Extended Data Fig. 2. The transition points were determined by the splitting of peaks.

For $\text{La}_3\text{Ni}_2\text{O}_7$, PDF analysis lacks sufficient sensitivity to pinpoint the phase boundary in tetragonal-orthorhombic transitions driven by octahedral rotations. Instead, here, the classical boundary was identified by the pressure where the derivative of the lattice parameter ratio c/a with respect to pressure becomes zero. This criterion works because at structural phase boundaries involving changes in crystal symmetry (like tetragonal to orthorhombic), the axial ratio c/a typically exhibits an extremum. The point where $d(\frac{c}{a})/dP_{\text{MD}} = 0$ thus marks the transition pressure where one structure becomes more stable than another. For each temperature and pressure, we performed a 6 ns MD simulation in the $4 \times 4 \times 1$ supercell. We used the NPT ensemble and the Langevin thermostat, with the friction factor being $\tau = 100$ fs. The results are summarized in the lower panel of Extended Data Fig. 2.

* xzli@pku.edu.cn

- [1] H. Ding, T. Yokoya, J. C. Campuzano, T. Takahashi, M. Randeria, M. R. Norman, T. Mochiku, K. Kadowaki, and J. Giapintzakis, Spectroscopic evidence for a pseudogap in the normal state of underdoped high-T_c superconductors, *Nature* **382**, 51 (1996).
- [2] K. Tanaka, W. S. Lee, D. H. Lu, A. Fujimori, T. Fujii, null, I. Terasaki, D. J. Scalapino, T. P. Devereaux, Z. Hussain, and Z.-X. Shen, Distinct fermi-momentum-dependent energy gaps in deeply underdoped Bi2212, *Science* **314**, 1910 (2006).
- [3] E. Razzoli, G. Drachuck, A. Keren, M. Radovic, N. C. Plumb, J. Chang, Y.-B. Huang, H. Ding, J. Mesot, and M. Shi, Evolution from a nodeless gap to $d_{x^2-y^2}$ -wave in underdoped $\text{La}_{2-x}\text{Sr}_x\text{CuO}_4$, *Phys. Rev. Lett.* **110**, 047004 (2013).
- [4] T. Timusk and B. Statt, The pseudogap in high-temperature superconductors: an experimental survey, *Rep. Prog. Phys.* **62**, 61 (1999).
- [5] M. Sigrist and K. Ueda, Phenomenological theory of unconventional superconductivity, *Rev. Mod. Phys.* **63**, 239 (1991).
- [6] M. R. Norman, The challenge of unconventional superconductivity, *Science* **332**, 196 (2011).
- [7] D. J. Scalapino, A common thread: The pairing interaction for unconventional superconductors, *Rev. Mod. Phys.* **84**, 1383 (2012).
- [8] G. R. Stewart, Unconventional superconductivity, *Adv. Phys.* **66**, 75 (2017).
- [9] C. Pellegrini and A. Sanna, Ab initio methods for superconductivity, *Nat. Rev. Phys.* **6**, 509 (2024).
- [10] H. Sun, M. Huo, X. Hu, J. Li, Z. Liu, Y. Han, L. Tang, Z. Mao, P. Yang, B. Wang, J. Cheng, D.-X. Yao, G.-M. Zhang, and M. Wang, Signatures of superconductivity near 80 K in a nickelate under high pressure, *Nature* **621**, 493 (2023).
- [11] J. Hou, P.-T. Yang, Z.-Y. Liu, J.-Y. Li, P.-F. Shan, L. Ma, G. Wang, N.-N. Wang, H.-Z. Guo, J.-P. Sun, Y. Uwatoko, M. Wang, G.-M. Zhang, B.-S. Wang, and J.-G. Cheng, Emergence of high-temperature superconducting phase in pressurized $\text{La}_3\text{Ni}_2\text{O}_7$ crystals, *Chin. Phys. Lett.* **40**, 117302 (2023).
- [12] Y. Zhu, D. Peng, E. Zhang, B. Pan, X. Chen, L. Chen, H. Ren, F. Liu, Y. Hao, N. Li, Z. Xing, F. Lan, J. Han, J. Wang, D. Jia, H. Wo, Y. Gu, Y. Gu, L. Ji, W. Wang, H. Gou, Y. Shen, T. Ying, X. Chen, W. Yang, H. Cao, C. Zheng, Q. Zeng, J.-g. Guo, and J. Zhao, Superconductivity in pressurized trilayer $\text{La}_4\text{Ni}_3\text{O}_{10-\delta}$ single crystals, *Nature* **631**, 531 (2024).
- [13] N. Wang, G. Wang, X. Shen, J. Hou, J. Luo, X. Ma, H. Yang, L. Shi, J. Dou, J. Feng, J. Yang, Y. Shi, Z. Ren, H. Ma, P. Yang, Z. Liu, Y. Liu, H. Zhang, X. Dong, Y. Wang, K. Jiang, J. Hu, S. Nagasaki, K. Kitagawa, S. Calder, J. Yan, J. Sun, B. Wang, R. Zhou, Y. Uwatoko, and J. Cheng, Bulk high-temperature superconductivity in pressurized tetragonal $\text{La}_2\text{PrNi}_2\text{O}_7$, *Nature* **634**, 579 (2024).
- [14] F. Li, Z. Xing, D. Peng, J. Dou, N. Guo, L. Ma, Y. Zhang, L. Wang, J. Luo, J. Yang, J. Zhang, T. Chang, Y.-S. Chen, W. Cai, J. Cheng, Y. Wang, Y. Liu, T. Luo, N. Hirao, T. Matsuoka, H. Kadobayashi, Z. Zeng, Q. Zheng, R. Zhou, Q. Zeng, X. Tao, and J. Zhang, Bulk superconductivity up to 96 K in pressurized nickelate single crystals, *Nature* **649**, 871 (2026).
- [15] M. Zhang, C. Pei, D. Peng, X. Du, W. Hu, Y. Cao, Q. Wang, J. Wu, Y. Li, H. Liu, C. Wen, J. Song, Y. Zhao, C. Li, W. Cao, S. Zhu, Q. Zhang, N. Yu, P. Cheng, L. Zhang, Z. Li, J. Zhao, Y. Chen, C. Jin, H. Guo, C. Wu, F. Yang, Q. Zeng, S. Yan, L. Yang, and Y. Qi, Superconductivity in trilayer nickelate $\text{La}_4\text{Ni}_3\text{O}_{10}$ under pressure, *Phys. Rev. X* **15**, 021005 (2025).
- [16] A. P. Drozdov, M. I. Eremets, I. A. Troyan, V. Ksenofontov, and S. I. Shylin, Conventional superconductivity at 203 kelvin at high pressures in the sulfur hydride system, *Nature* **525**, 73 (2015).
- [17] D. Duan, Y. Liu, F. Tian, D. Li, X. Huang, Z. Zhao, H. Yu, B. Liu, W. Tian, and T. Cui, Pressure-induced metallization of dense $(\text{H}_2\text{S})_2\text{H}_2$ with high-T_c superconductivity, *Sci. Rep.* **4**, 6968 (2014).
- [18] A. P. Drozdov, P. P. Kong, V. S. Minkov, S. P. Besedin, M. A. Kuzovnikov, S. Mozaffari, L. Balicas, F. F. Balakirev, D. E. Graf, V. B. Prakapenka, E. Greenberg, D. A. Knyazev, M. Tkacz, and M. I. Eremets, Superconductivity at 250 K in lanthanum hydride under high pressures, *Nature* **569**, 528 (2019).
- [19] I. Errea, M. Calandra, C. J. Pickard, J. R. Nelson, R. J. Needs, Y. Li, H. Liu, Y. Zhang, Y. Ma, and F. Mauri, Quantum hydrogen-bond symmetrization in the superconducting hydrogen sulfide system, *Nature* **532**, 81 (2016).
- [20] M. Einaga, M. Sakata, T. Ishikawa, K. Shimizu, M. I. Eremets, A. P. Drozdov, I. A. Troyan, N. Hirao, and Y. Ohishi, Crystal structure of the superconducting phase of sulfur hydride, *Nat. Phys.* **12**, 835 (2016).
- [21] Y. Yuan, Y. Feng, L. Bian, D.-B. Zhang, and X.-Z. Li,

The quantum nature of the superconducting hydrogen sulfide at finite temperatures (2016), arXiv:1607.02348.

[22] Y.-C. Zhu, J.-X. Zeng, Q.-J. Ye, and X.-Z. Li, Quantum Disorder Induced by Nuclear Tunneling in Lattice, *Phys. Rev. Lett.* **134**, 246401 (2025).

[23] L. Wang, Y. Li, S.-Y. Xie, F. Liu, H. Sun, C. Huang, Y. Gao, T. Nakagawa, B. Fu, B. Dong, Z. Cao, R. Yu, S. I. Kawaguchi, H. Kadobayashi, M. Wang, C. Jin, H.-k. Mao, and H. Liu, Structure Responsible for the Superconducting State in $\text{La}_3\text{Ni}_2\text{O}_7$ at High-Pressure and Low-Temperature Conditions, *J. Am. Chem. Soc.* **146**, 7506 (2024).

[24] V. S. Minkov, V. B. Prakapenka, E. Greenberg, and M. I. Eremets, A boosted critical temperature of 166 K in superconducting D3S synthesized from elemental sulfur and hydrogen, *Angew. Chem. Int. Ed.* **59**, 18970 (2020).

[25] D. Chandler and P. G. Wolynes, Exploiting the isomorphism between quantum theory and classical statistical mechanics of polyatomic fluids, *J. Chem. Phys.* **74**, 4078 (1981).

[26] D. Marx and M. Parrinello, Ab initio path integral molecular dynamics: Basic ideas, *J. Chem. Phys.* **104**, 4077 (1996).

[27] T. E. Markland and M. Ceriotti, Nuclear quantum effects enter the mainstream, *Nat. Rev. Chem.* **2**, 0109 (2018).

[28] S. Sachdev, *Quantum Phase Transitions*, 2nd ed. (Cambridge University Press, 2011).

[29] C. Cazorla and J. Boronat, Simulation and understanding of atomic and molecular quantum crystals, *Rev. Mod. Phys.* **89**, 035003 (2017).

[30] J. Cao and G. A. Voth, The formulation of quantum statistical mechanics based on the Feynman path centroid density. I. Equilibrium properties, *J. Chem. Phys.* **100**, 5093 (1994).

[31] S. Jang and G. A. Voth, Path integral centroid variables and the formulation of their exact real time dynamics, *J. Chem. Phys.* **111**, 2357 (1999).

[32] J. Behler and M. Parrinello, Generalized Neural-Network Representation of High-Dimensional Potential-Energy Surfaces, *Phys. Rev. Lett.* **98**, 146401 (2007).

[33] E. Kocer, T. W. Ko, and J. Behler, Neural Network Potentials: A Concise Overview of Methods, *Annu. Rev. Phys. Chem.* **73**, 163 (2022).

[34] J. P. Perdew, K. Burke, and M. Ernzerhof, Generalized gradient approximation made simple, *Phys. Rev. Lett.* **77**, 3865 (1996).

[35] L. Monacelli, R. Bianco, M. Cherubini, M. Calandra, I. Errea, and F. Mauri, The stochastic self-consistent harmonic approximation: calculating vibrational properties of materials with full quantum and anharmonic effects, *J. Phys.: Condens. Matter* **33**, 363001 (2021).

[36] R. Akashi, M. Kawamura, S. Tsuneyuki, Y. Nomura, and R. Arita, First-principles study of the pressure and crystal-structure dependences of the superconducting transition temperature in compressed sulfur hydrides, *Phys. Rev. B* **91**, 224513 (2015).

[37] Z. Huo, Z. Luo, P. Zhang, A. Yang, Z. Liu, X. Tao, Z. Zhang, S. Guo, Q. Jiang, W. Chen, D.-X. Yao, D. Duan, and T. Cui, Modulation of the octahedral structure and potential superconductivity of $\text{La}_3\text{Ni}_2\text{O}_7$ through strain engineering, *Sci. China- Phys. Mech. Astron.* **68**, 237411 (2025).

[38] A. Damascelli, Z. Hussain, and Z.-X. Shen, Angle-resolved photoemission studies of the cuprate superconductors, *Rev. Mod. Phys.* **75**, 473 (2003).

[39] P. Dai, Antiferromagnetic order and spin dynamics in iron-based superconductors, *Rev. Mod. Phys.* **87**, 855 (2015).

[40] N. P. Armitage, P. Fournier, and R. L. Greene, Progress and perspectives on electron-doped cuprates, *Rev. Mod. Phys.* **82**, 2421 (2010).

[41] C.-Q. Chen, W. Qiu, Z. Luo, M. Wang, and D.-X. Yao, Electronic structures and superconductivity in Nd-doped $\text{La}_3\text{Ni}_2\text{O}_7$, *Sci. China- Phys. Mech. Astron.* **69**, 247414 (2026).

[42] B. Sun, S. Niu, R. P. Hermann, J. Moon, N. Shulumba, K. Page, B. Zhao, A. S. Thind, K. Mahalingam, J. Milam-Guerrero, R. Haiges, M. Mecklenburg, B. C. Melot, Y.-D. Jho, B. M. Howe, R. Mishra, A. Alatas, B. Winn, M. E. Manley, J. Ravichandran, and A. J. Minnich, High frequency atomic tunneling yields ultralow and glass-like thermal conductivity in chalcogenide single crystals, *Nat. Commun.* **11**, 6039 (2020).

[43] A. Togo, L. Chaput, T. Tadano, and I. Tanaka, Implementation strategies in phonopy and phono3py, *J. Phys. Condens. Matter* **35**, 353001 (2023).

[44] Y. Litman, V. Kapil, Y. M. Y. Feldman, D. Tisi, T. Begušić, K. Fidanyan, G. Fraux, J. Higer, M. Kellner, T. E. Li, E. S. Pós, E. Stocco, G. Trenins, B. Hirshberg, M. Rossi, and M. Ceriotti, i-PI 3.0: A flexible and efficient framework for advanced atomistic simulations, *J. Chem. Phys.* **161**, 062504 (2024).

[45] G. Kresse and J. Furthmüller, Efficiency of ab-initio total energy calculations for metals and semiconductors using a plane-wave basis set, *Comput. Mater. Sci.* **6**, 15 (1996).

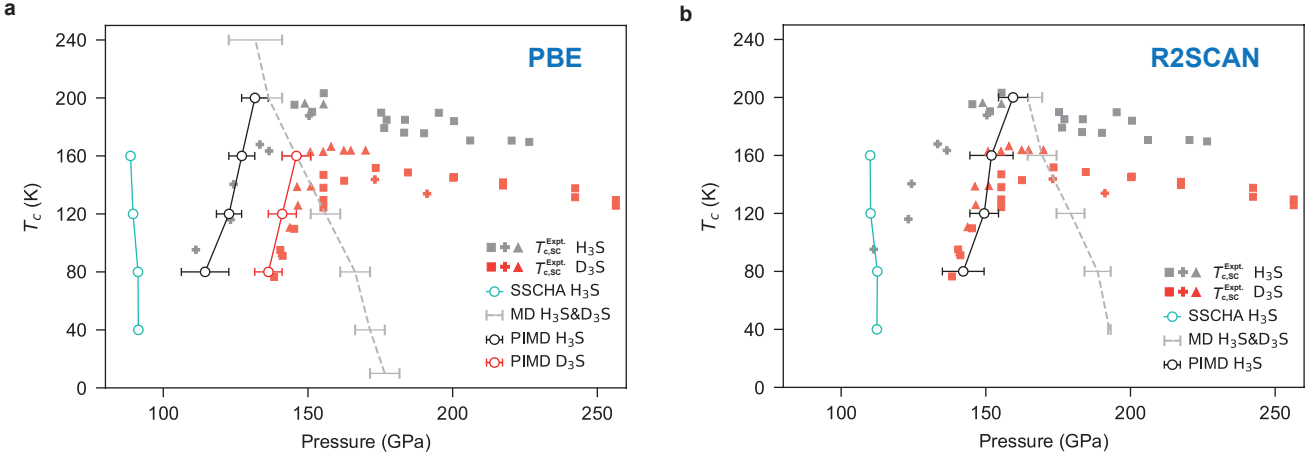
[46] G. Kresse and D. Joubert, From ultrasoft pseudopotentials to the projector augmented-wave method, *Phys. Rev. B* **59**, 1758 (1999).

[47] Y.-C. Zhu, S. Yang, J.-X. Zeng, W. Fang, L. Jiang, D. H. Zhang, and X.-Z. Li, Torsional tunneling splitting in a water trimer, *J. Am. Chem. Soc.* **144**, 21356 (2022).

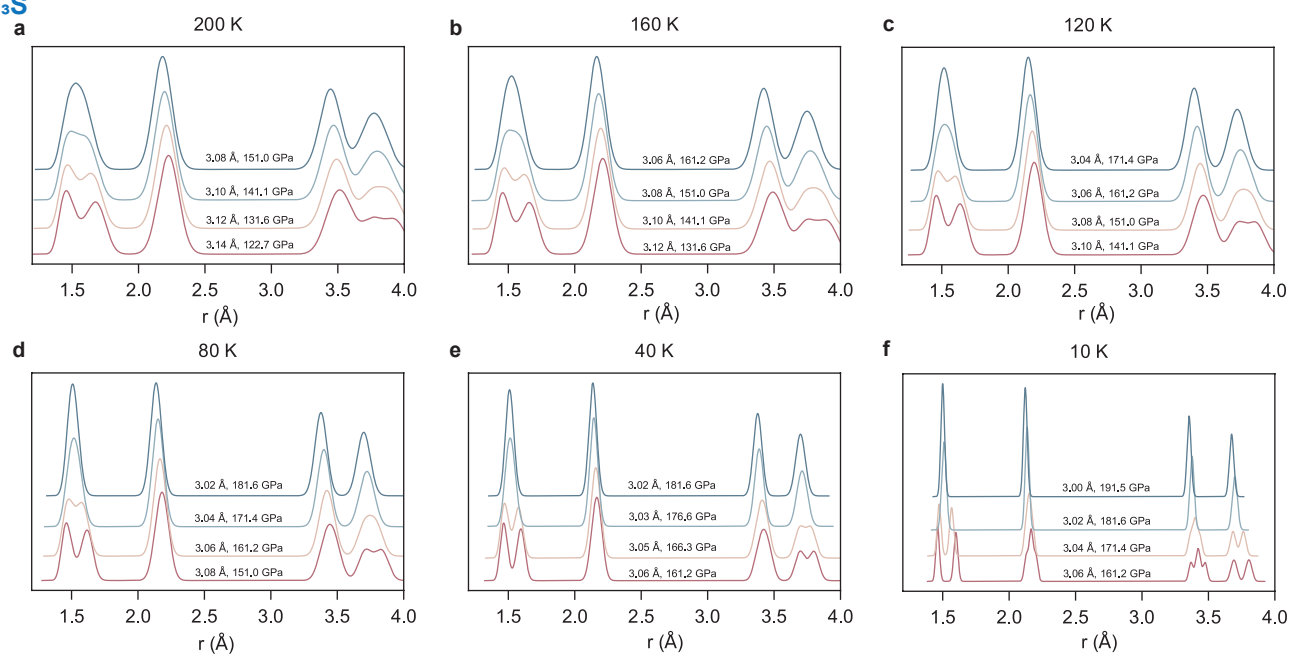
[48] R. Jinnouchi, J. Lahnsteiner, F. Karsai, G. Kresse, and M. Bokdam, Phase transitions of hybrid perovskites simulated by machine-learning force fields trained on the fly with bayesian inference, *Phys. Rev. Lett.* **122**, 225701 (2019).

[49] R. Jinnouchi, F. Karsai, C. Verdi, R. Asahi, and G. Kresse, Descriptors representing two- and three-body atomic distributions and their effects on the accuracy of machine-learned inter-atomic potentials, *J. Chem. Phys.* **152**, 234102 (2020).

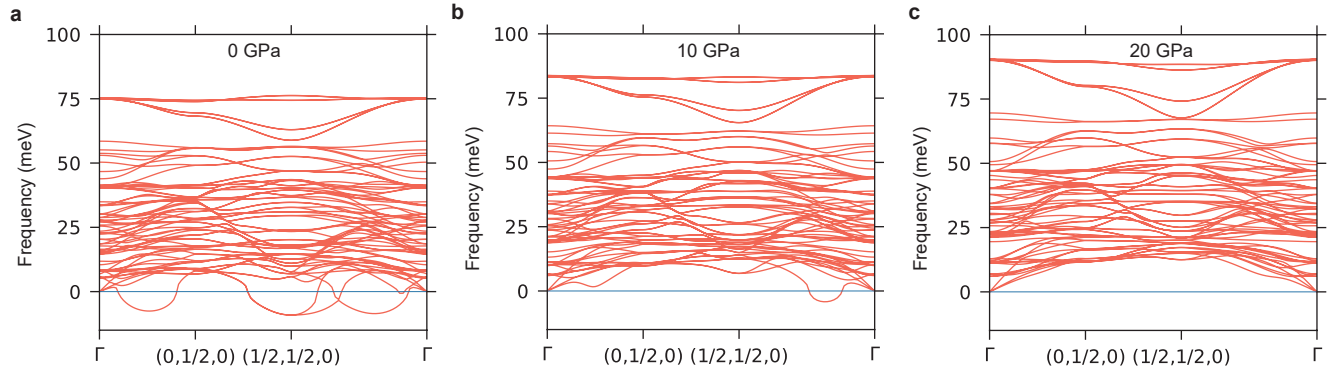
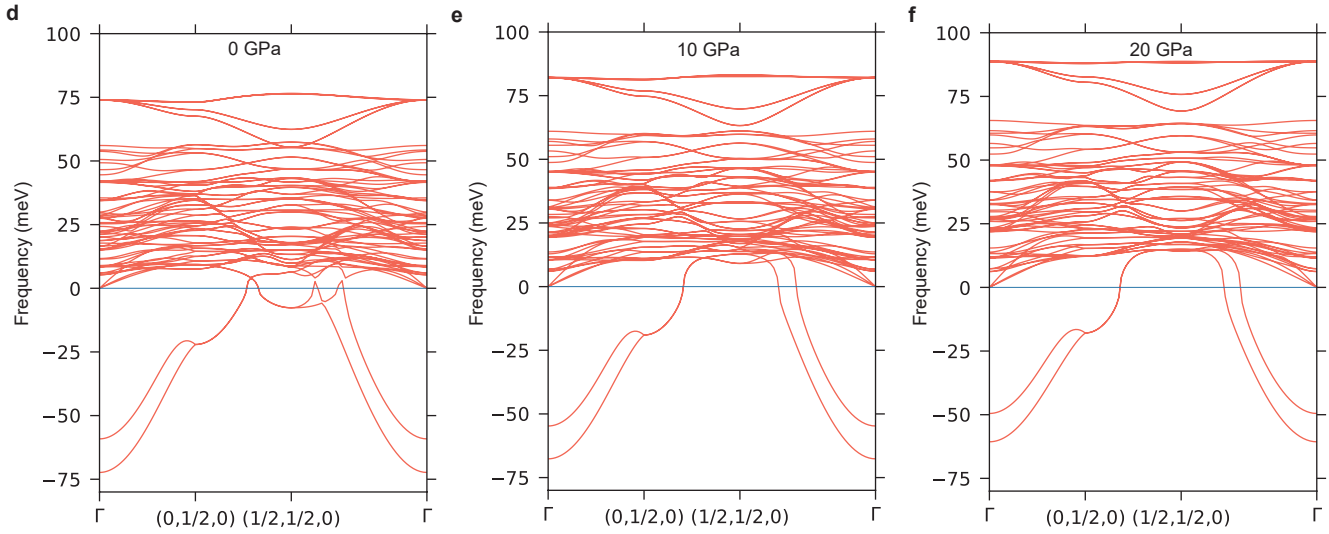
[50] M. Ceriotti, M. Parrinello, T. E. Markland, and D. E. Manolopoulos, Efficient stochastic thermostating of path integral molecular dynamics, *J. Chem. Phys.* **133**, 124104 (2010).



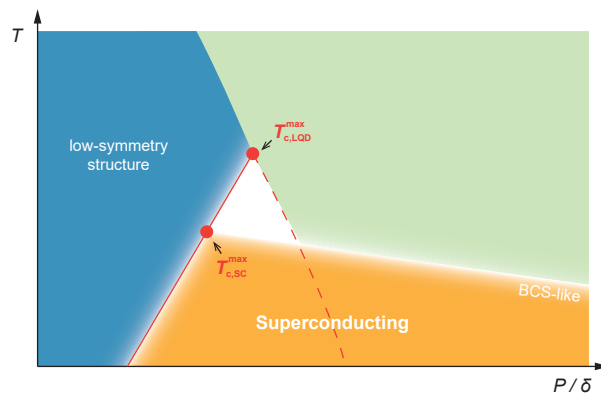
Extended Data Fig. 1: **LQD phase and the SSCHA phase boundary in H_3S by different functionals.** The structural phase boundary between $\text{Im}\bar{3}\text{m}$ (high-pressure) and $\text{R}3\text{m}$ (low-pressure) by the stochastic self-consistent harmonic approximation (SSCHA) method[35] is shown by the cyan line. SSCHA predicts a much lower transition pressure compared to PIMD. In comparison with PBE, the structural phase boundary by R2SCAN functional shifts to higher pressure because, at the same pressure, R2SCAN predicts a higher potential barrier hence weaker quantum fluctuation.

H₃S

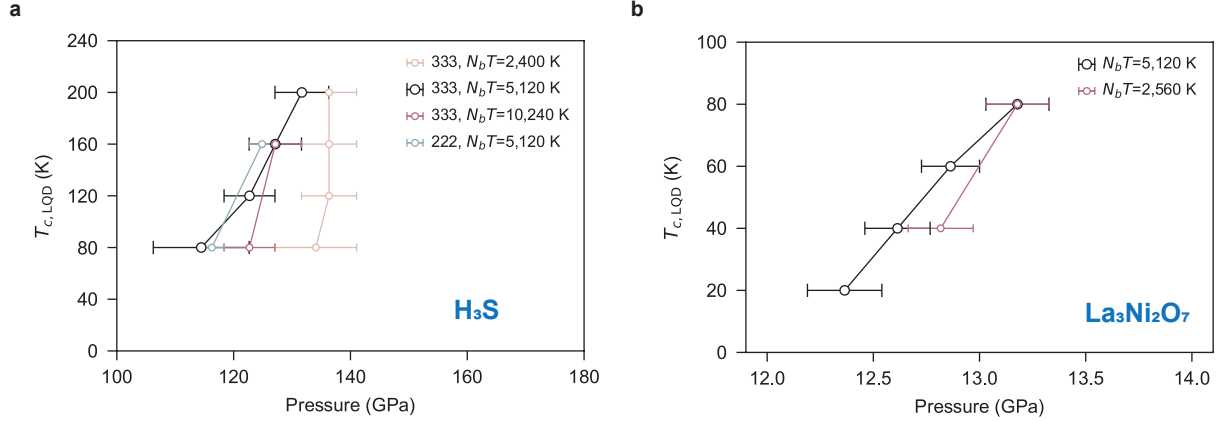
Extended Data Fig. 2: **Classical structural phase boundaries by MD.** **a-f**, S-H pair distribution function for H₃S at different temperatures and pressures. The PDFs obtained from MD are identical for D₃S and H₃S. **g**, pair distribution function for La₃Ni₂O₇. **h**, derivative of the lattice parameter ratio c/a with respect to pressure. **i**, PIMD predicts a higher pressure than MD at the same volume. **j**, the classical transition pressure was determined by $d(\frac{c}{a})/dP_{MD} = 0$.

PBE+U=4**PBE+U=6**

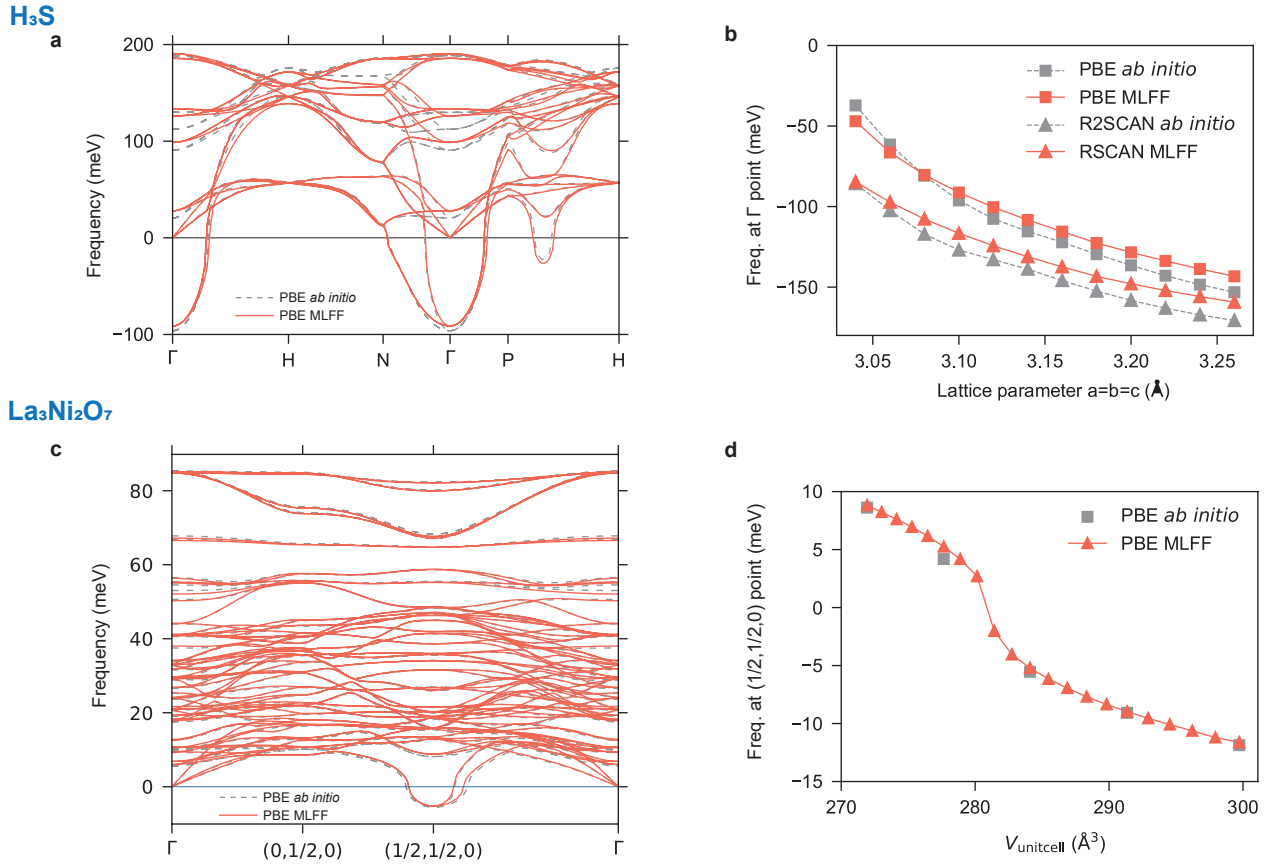
Extended Data Fig. 3: **Harmonic phonon spectra of $\text{La}_3\text{Ni}_2\text{O}_7$ by PBE+U.** **a-c**, Hubbard $U = 4.0$ eV at 0, 10 and 20 GPa. **d-f**, Hubbard $U = 6.0$ eV at 0, 10 and 20 GPa.



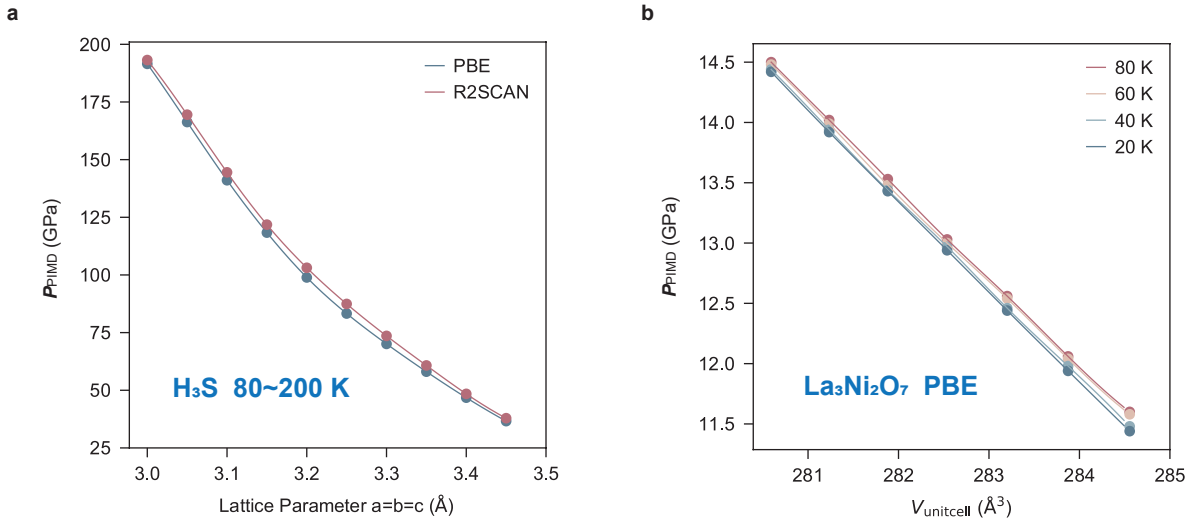
Extended Data Fig. 4: **Schematic diagram of another possible phase diagram.**



Extended Data Fig. 5: **Convergence on number of beads N_b and size of supercell in PIMD simulation.** **a**, the PIMD phase boundaries of H₃S when $N_b \times T = 2,400, 5,120$ and 10,240 K in a 3 × 3 × 3 or 2 × 2 × 2 supercell of unit cell. **b**, the PIMD phase boundaries of La₃Ni₂O₇ when $N_b \times T = 2,560$ and 5,120 K.



Extended Data Fig. 6: **Comparison of MLFF PES and ab initio PES.** **a**, harmonic phonon spectra of H₃S at $P_{\text{PIMD}} = 141$ Gpa (lattice parameter $a = 3.10$ Å). **b**, frequency of soft mode at Γ point when varying lattice parameter. **c**, harmonic phonon spectra of La₃Ni₂O₇ at $V_{\text{unitcell}} = 384.1$ Å³. **d**, frequency of soft mode at (1/2, 1/2, 0) k -point when varying volume.



Extended Data Fig. 7: **P-V curves for H_3S (a) and $\text{La}_3\text{Ni}_2\text{O}_7$ (b).**